The Astrophysical Journal Letters, 834:L21 (5pp), 2017 January 10 doi:10.3847/2041-8213/834/2/L21

Experimental Observation of Thin-shell Instability in a Collisionless Plasma

H. Ahmed[1], D. Doria[1], M. E. Dieckmann[2], G. Sarri[1], L. Romagnani[3], A. Bret[4,5], M. Cerchez[6], A. L. Giesecke[6], E. Ianni[1], S. Kar[1], M. Notley[7], R. Prasad[6], K. Quinn[1], O. Willi[6], and M. Borghesi[1]
[1] Centre for Plasma Physics, Queen's University of Belfast, Belfast BT7 1NN, UK; d.doria@qub.ac.uk, m.borghesi@qub.ac.uk
[2] Department of Science and Technology, Linkoping University, SE-60174 Norrkoping, Sweden
[3] LULI, École Polytechnique, CNRS, CEA, UPMC, Palaiseau, France
[4] ETSI Industriales, Universidad Castilla La Mancha, E-13 071 Ciudad Real, Spain
[5] Instituto de Investigaciones Energticas y Aplicaciones Industriales, Campus Universitario de Ciudad Real, E-13071 Ciudad Real, Spain
[6] Institute for Laser and Plasma Physics, University of Düsseldorf, Germany
[7] Central Laser Facility, Rutherford Appleton Laboratory, Chilton, Oxfordshire OX11 0QX, UK
Received 2016 November 17; accepted 2016 December 10; published 2017 January 12

Abstract

We report on the experimental observation of the instability of a plasma shell, which formed during the expansion of a laser-ablated plasma into a rarefied ambient medium. By means of a proton radiography technique, the evolution of the instability is temporally and spatially resolved on a timescale much shorter than the hydrodynamic one. The density of the thin shell exceeds that of the surrounding plasma, which lets electrons diffuse outward. An ambipolar electric field grows on both sides of the thin shell that is antiparallel to the density gradient. Ripples in the thin shell result in a spatially varying balance between the thermal pressure force mediated by this field and the ram pressure force that is exerted on it by the inflowing plasma. This mismatch amplifies the ripples by the same mechanism that drives the hydrodynamic nonlinear thin-shell instability (NTSI). Our results thus constitute the first experimental verification that the NTSI can develop in colliding flows.

Key words: instabilities – plasmas – shock waves

Supporting material: animation

1. Introduction

The boundaries that form when a stellar wind or outflow collides with the interstellar medium (ISM) are prone to hydrodynamic instabilities. An example for an unstable collision boundary is that between the ISM and the material that has been accelerated by a supernova (SN) explosion. The forward shock that ensheaths the SN blast shell sweeps up the ISM and accumulates material behind it. The compressed ISM is initially separated from the blast-shell material by a contact discontinuity. In time, a reverse shock forms that propagates backward in the direction of the progenitor star.

Chevalier et al. (1992) discuss how the Rayleigh–Taylor instability can destabilize the contact discontinuity and how this destabilization affects the reverse shock. Prior to the formation of the reverse shock, the expanding shell can also be destabilized by the linear thin-shell instability (Vishniac 1983; Ryu & Vishniac 1987; van Marle et al. 2011; van Marle & Keppens 2012). It is thought that the disruption of the blast-shell front by these instabilities gives rise to the intricate density and flow patterns displayed by some SN remnants.

Once the reverse shock has developed, the SN blast shell is enwrapped by a dense thin shell, which is separated by hydrodynamic shocks from the unperturbed ISM and from the trailing blast-shell material. This thin shell is stable against linear instabilities but not necessarily against the nonlinear thin-shell instability (NTSI; Vishniac 1994). The NTSI has been studied with hydrodynamic (Folini et al. 2014) and magneto-hydrodynamic (Heitsch et al. 2007; McLeod & Whitworth 2013) simulations. However, unlike Rayleigh–Taylor or linear thin-shell instabilities (Grun et al. 1991; Edens et al. 2005; Ditmire & Edens 2008), the NTSI in a fluid or plasma has not yet been detected experimentally. The lack of experimental observations so far is presumably tied to the difficulty with creating a thin rippled shell of fluid or plasma that is confined by a shock on either side. Recently, Dieckmann et al. (2015) showed that the hydrodynamic NTSI has an analog in collisionless plasma. The shocks are substituted by ambipolar electric fields but the instability mechanism is the same in both cases.

We present here the experimental observation of a thin shell of collisionless plasma that forms at the surface of a laser-generated blast shell as it expands into a low-density plasma. The measured electric field profiles strengthen the case for it to be an NTSI. The spatial oscillations along the shell are observed to grow in time with an approximately constant wavelength. We verify by means of particle-in-cell (PIC) simulations that the NTSI can develop at this wavelength. Moreover, the growth rate predicted by a simple analytical model is in good agreement with the experimental results and with the predictions by Vishniac (1994). Our experimental results constitute the first experimental observation of the NTSI in a colliding flow.

2. Experimental Arrangement

The experiment was carried out using the VULCAN laser facility at the Rutherford Appleton Laboratory (Danson et al. 1998), using the setup shown in Figure 1(a). A laser pulse of duration ∼1 ns and energy ∼ 70 J, was focused onto a 50 μm thick gold foil, at an incidence angle of ∼45° to a peak intensity of $\sim 10^{15}$ W cm^{-2}. The interaction of the nanosecond pulse with the gold foil leads to the generation of ablated plasma that is mainly constituted of thermally distributed gold ions and faster lighter ions with an average energy per nucleon of tens of keV (Tan et al. 1984; Gitomer et al. 1986). The lighter ions, such as protons and carbon ions, originate from contaminant layers (water vapor and hydrocarbon) typically

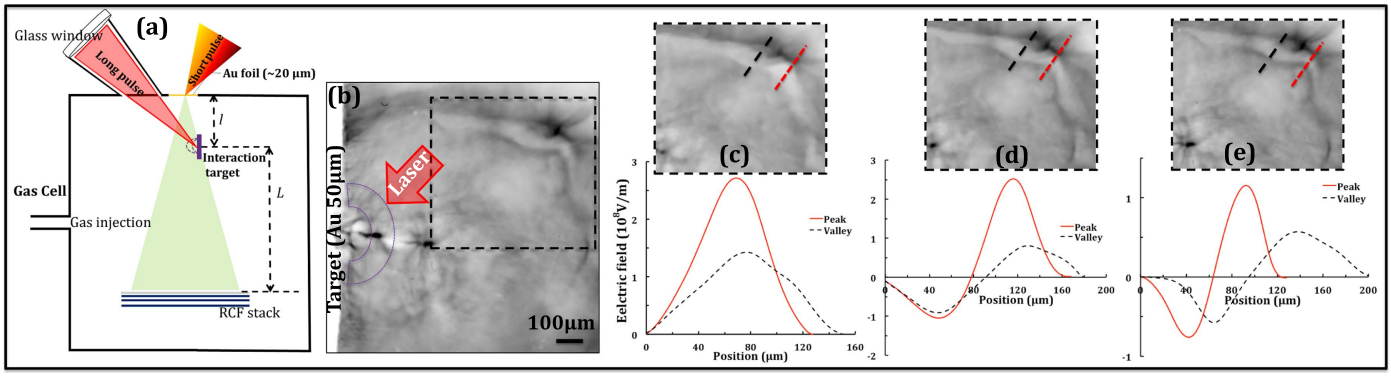

Figure 1. (a) Schematic of the experimental setup (top view). The experimental setup was enclosed in a gas cell, which was placed inside the vacuum chamber. (b) Proton radiographs of the interaction of a nanosecond laser pulse (red arrow), with a 50 μm thick gold foil, correspond to time $(t_0 + 6)$ ps from the start of interaction. The spatial scale shown in panel (b) corresponds to the object plane. Panels (c)–(e) show the radiographs of the interested region (marked in panel (b)), and reconstructed electric field profiles at different positions across the plasma shell correspond to different probing times t_0, $(t_0 + 2)$ ps, $(t_0 + 6)$ ps.

present on the surface of the targets (Gitomer et al. 1986). The laser–target interaction was enclosed in a gas cell filled with pure nitrogen at a controlled pressure of $\sim 10^{-1}$ mbar. Hydrodynamic simulations using the code HYADES (Larsen & Lane 1994) indicate that the gas becomes fully ionized within 100 ps from the start of the laser irradiation by the X-rays emitted from the target (Dean et al. 1971), resulting in a stationary plasma with an electron density and temperature of $\sim 3 \times 10^{16}$ cm^{-3} and $T_e \sim 1$ keV, respectively. These values imply an electron Debye length of $\lambda_D \sim 1.4$ μm and an ion-acoustic speed of $C_s \sim 2.2 \times 10^5$ m s^{-1}. Moreover, the Coulomb logarithm for electron–electron and ion–ion collisions are of the order of 6 and 11, respectively, indicating a characteristic timescale for collisions of $\tau_{ee} \sim 36$ ns and $\tau_{ii} \sim 600$ ns, respectively. The PPI technique (Borghesi et al. 2002; Sarri et al. 2010) was employed to investigate the interaction of the ablated plasma with the background plasma. The probe proton beam was generated by focusing a second laser pulse of $\sim$1 ps duration and $\sim$50 J energy, to an intensity of $\sim 10^{19}$ W cm^{-2} onto a thin gold foil (thickness $\sim$20 μm). In the experimental arrangement shown in the Figure 1(a), the distance between proton source and interaction region was $l \simeq 4$ mm, and the detector was placed at $L \simeq 38$ mm from the interaction region, giving an intrinsic geometrical magnification of $M \approx (l + L)/l \sim 10.5$ (Borghesi et al. 2002). A stack of several layers of dosimetrically calibrated (Kirby et al. 2011) RadioChromic Films (RCF), was used to detect the proton beam. The two lasers were temporally delayed so that a proton with an energy of 13 MeV traverses the interaction region at the time $t_0 = 180 \pm 20$ ps after the start of the long-pulse irradiation, where the start of the interaction corresponds to 1/10 of the peak intensity. The error in defining the beginning of the interaction is mainly due to the systematic error in the synchronization of both laser beams. This does not affect the temporal resolution of the PPI technique, which is on the order of picoseconds (Sarri et al. 2010).

3. Results and Discussion

Figure 1(b) shows a characteristic proton radiograph of the interaction. The white shadow on the left of the image indicates the position of the solid target and the ns laser beam incidence direction is marked by a red arrow. Ahead of the plasma in the vicinity of the solid target, a pronounced modulation in the probe proton density (two darker lines of proton accumulation separated by a stripe of proton depletion) is clearly visible, at approximately 900 microns from the laser interaction point. As a rule of thumb, the electric fields are directed from the regions of a lighter gray color compared to the background (zones of reduced probe proton flux) toward the regions of darker gray color (increased flux). A series of zoomed RCF images of this structure (obtained within the same laser shot) are shown in panels (c)–(e), which correspond, respectively, to t_0, $t_0 + 2$ ps, and $t_0 + 6$ ps. Such a modulation can be interpreted as a thin plasma shell, bounded by double layers or electrostatic shocks (Hershkowitz 1981; Ahmed et al. 2013). Furthermore, a pronounced periodic spatial oscillation along the thin shell can also be seen in Figure 1(c), similar to the perturbations observed on the surface of a blast wave (Edens et al. 2005) in hydrodynamically expanding plasma. These spatial oscillations along the shell have been observed repeatedly in the experiment. Numerical simulations of similar scenarios demonstrated that the presence of background plasma restrains the generation of magnetic field (Sarri et al. 2011), allowing one to assume that the proton deflections observed on the RCF are solely related to electrostatic fields. Under this assumption, the electric field responsible for the proton deflections can be analytically estimated (Sarri et al. 2010) as long as protons are subject to small angular deflections. The extracted electric field profiles are shown in Figures 1(c)–(e), indicating that the electric field evolves from a bell-shaped profile to an asymmetric bipolar profile, while maintaining a peak amplitude of the order of 100 MV m^{-1}. The potential associated with the thin shell is of the order of a kV that, while being sufficiently strong to reflect the nitrogen ions of the background plasma has a small effect on the multi-MeV probing protons, confirming that the formation of caustics (as discussed in Kugland et al. 2012) has no relevance here.

With respect to the frame shown in Figure 1(c), where the spatial oscillations along the thin shell are not clearly visible, these become more pronounced in the following frames (Figures 1(d) and (e)), showing how the shell front becomes corrugated in a few picoseconds (i.e., on a timescale much smaller than the inverse of the ion plasma frequency), while preserving a roughly constant oscillation period of $\lambda_{\rm osc} \sim 275 \pm 20$ μm. Detailed analysis of the evolution of the corrugated front indicates that the shell velocity varies significantly along the shell. It is found that the crests move with velocity $v \sim (1.5 \pm 0.3) \times 10^6$ m s^{-1}, corresponding to a Mach number of $\sim$7, which is almost twice the velocity of the

valleys. The shell speed, measured in the reference frame that moves with the average speed of the shell, thus reaches a peak value that is comparable to the ion-acoustic speed. Moreover, the thickness of the thin shell at the crest is approximately 45 μm $\sim 30\lambda_{De}$, almost half of the thickness at the trough of the wiggles. It is important to note here that the timescale over which this structure evolves is much smaller than the average electron–electron and ion–ion collision times allowing one to assume that the dynamics of the plasma is purely collisionless.

The modulation of the thin shell observed in the experimental data, cannot be caused by a spatially varying plasma flow velocity or density profile. Significant variations of the plasma density or convection speed could be introduced, in principle, close to the target by an imperfect shape of the laser pulse or the target. However, the source of the ablated plasma can effectively be considered a point-like source (40 μm compared to approximately 900 μm at which the structure is observed) and such initial variations would be negligible.

An initial nonuniform plasma flow close to the laser-ablated target could only cause the observed spatial oscillations of the thin shell, if the latter would be amplified by an instability. A plausible scenario can be envisaged starting from a thin plasma shell enclosed by two rippled double layers. The thin shell is created by the collision of two plasma clouds. Binary collisions between plasma particles are negligible and both clouds interpenetrate. Their cumulative density exceeds that of the surrounding clouds, which form the inflowing upstream medium. Thermal diffusion results in a net outflow of electrons from the dense shell, which is eventually canceled by an ambipolar electric field. The electric field traps the electrons within the thin shell. It slows down the inflowing upstream ions in the direction of the density gradient in the same way as the inflowing upstream medium is slowed down only along the normal of a hydrodynamic shock. The thermal pressure gradient force, which is imposed by the dense thin shell on the upstream medium, and the density gradient are antiparallel in the collisionless and in the hydrodynamic case. If the thin shell is rippled, then the thermal pressure gradient force and the ram pressure force are no longer antiparallel everywhere along the shell. Vishniac (1994) demonstrated that ripples with a sufficiently large amplitude can destabilize the thin shell if the ripples follow the shape of the letter s.

On a microscopic level, the growth mechanism of the collisionless NTSI is understood best if we consider a thin shell that is displaced in an approximately sinusoidal fashion along the average normal of the double layers and if the velocity of the inflowing upstream fluid is spatially uniform on either side of the thin shell. The angle between the double layer normal and the upstream flow velocity vector varies along the rippled thin shell. The velocity component along the double layer normal of the upstream fluid is then reduced by the crossing, while the lateral velocity remains unchanged. The consequence is a rotation of the ion velocity vector by the shock crossing at an angle that varies with the position along the shock boundary. The ions from one upstream flow are deflected to the crests that propagate in the same direction as the upstream flow from which they originate, which increases the momentum modulus at the crests. The redistribution thus reinforces the initial spatial oscillation of the thin shell, thus giving rise to an instability, whereby ions are piled up at the co-moving crest of the oscillations.

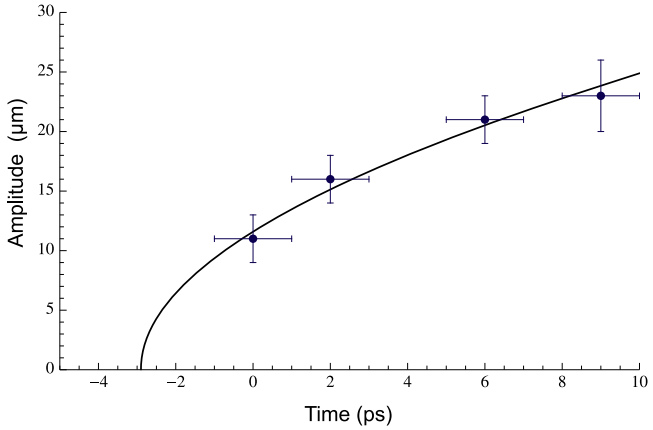

Figure 2. Temporal evolution of the amplitude of the corrugation on the front of the plasma shell. The uncertainties in amplitude and time are due to the nonzero size of the virtual source of the proton beam and the spectral acceptance of each RCF film, respectively (see Sarri et al. 2010 for details).

In order to understand the growth of the corrugation, we have developed a simple analytical model, which estimates the rate of mass accumulation at the crests of the oscillations for a sinusoidally varying front (see Doria et al. 2016 for details). By assuming that the ion flow within the shell remains subsonic (no shocks) and that the amplitude of the oscillation $A(t)$ and the thickness of the shell are smaller than the spatial period of the oscillation $\lambda_{\rm osc}$, the amplitude is expected to grow in time as

$$A(t) \approx \frac{\lambda_{\rm osc}}{\pi} \times \sqrt{\frac{2n_0 v_0 (t - t_0) + (d_0\rho_0 - d\rho)}{d\rho}}, \qquad (1)$$

where, d, v_0, n_0, and ρ are the average thickness, the velocity of the inflowing plasmas in the reference frame of the shell, background ion density, and mass density of the shell, respectively. Using experimental values for velocity, thickness, and wavelength, the predicted growth is in good agreement with the experimental data (see Figure 2).

4. Simulations

We verify with PIC simulations using the EPOCH code (Arber et al. 2015) that the instability grows on the observed timescales. We let two initially separated plasma clouds collide. Both clouds are equally dense and they are in contact at a collision boundary, which is on average orthogonal to the collision direction. We impose a small sinusoidal displacement of the boundary along the collision direction that seeds the TSI. Each plasma cloud is spatially uniform and consists of electrons and protons with the mass ratio $m_p/m_e = 1836$ and the same number density $n_0 = 3 \times 10^{16}\,{\rm cm}^{-3}$. Both species move at the same mean speed. We set the electric and magnetic fields to zero at the time $t = 0$. The electron and proton temperatures are $T_e = 1\,{\rm keV}$ and $T_p = T_e/5$. The electron plasma frequency is $\omega_p \approx 10^{13}\,{\rm s}^{-1}$. The plasma cloud 1 moves with the speed $v_0 = 1.75 \times 10^6\,{\rm m\,s}^{-1}$ along x, and it collides with plasma cloud 2, which is at rest in the simulation frame. A dense plasma shell will form close to the initial collision boundary due to the overlapping of both clouds. Its center propagates toward increasing x with a mean speed $v_0/2 \approx 9 \times 10^5\,{\rm m\,s}^{-1}$ that is close to the shell's speed in the experiment. The assumption of a planar shell in the simulations is well justified by the quasi-planarity of the oscillations in the

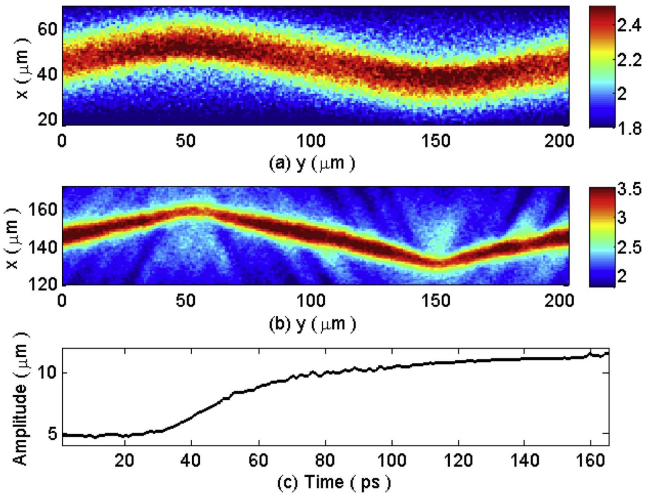

Figure 3. Panels (a) and (b) show the proton density at $t = 50$ ps and $t = 165$ ps and are expressed in units of the initial density n_0. Panel (c) evidences the growth of the amplitude $x_B(k_0, t)$ of the boundary oscillation.

(An animation of this figure is available.)

experimental data (compare a typical amplitude of the corrugation of tens of microns with the radius of the shell of the order of 900 microns). The simulation box resolves the x-interval $-L_x/2 \leqslant x \leqslant L_x/2$ with $L_x = 1.02$ mm and the y-interval $0 \leqslant y \leqslant L_y$ with $L_y = 204\ \mu$m using 1250×250 grid cells. The boundary conditions are periodic along y. The boundary at $x = -L_x/2$ is open and the one at $x = L_x/2$ is reflecting. The contact boundary at $x_B(y, t) = 4.9 \sin(2\pi y/L_y)\ \mu$m separates the plasma cloud 1 with $x < x_B$ from the plasma cloud 2 with $x > x_B$ at $t = 0$. Electrons and protons are represented by 250 computational particles per cell, respectively.

Figure 3 shows the proton density distributions at t = 50 ps and 165 ps as well as the amplitude of the oscillation $x_B(k_0, t)$ of the boundary with the wavenumber $k_0 = 2\pi/L_y$. We determine $x_B(k_0, t)$ as follows. We extract two contour lines $x_{\min}(y, t)$ and $x_{\max}(y, t)$ from the proton density distribution. Both contour lines are defined by $0.85\ n_{\max}(t)$, where $n_{\max}(t)$ is the proton's peak density at the time t. The thin shell is bounded by $x_{\min}(y, t)$ at low values of x and by $x_{\max}(y, t)$ at large values. We use these contour lines to compute $x_B(y, t) = [x_{\min}(y, t) + x_{\max}(y, t)]/2$ for $t > 0$. We Fourier transform $x_B(y, t)$ along y and extract $x_B(k_0, t)$. The proton density is animated in time in the animation of Figure 3. The proton distribution at $t = 50$ ps reveals a thin shell with a density $\approx 2.3 n_0$. Its center of mass along x is located at about 45 μm, and it has thus propagated at the speed $v_0/2$ along this direction. The shell's oscillation follows that of $x_B(y, t)$, but its amplitude is larger than 4.9 μm. Figure 3(c) reveals that it has increased to 7.5 μm. An amplitude increase by about 2.5 μm during 20 ps implies that the boundary speed at the extremities is about $1.25 \times 10^5\ \mathrm{m\,s^{-1}}$ or about one-fourth of the ion-acoustic speed, which is well below that observed in the experiment.

The strength of the ambipolar electric field, and thus the angle at which the ion velocity is rotated by the double layer crossing, depends on the ratio between the collision speed and the ion-acoustic speed (Dieckmann et al. 2013), on how the density of the laser-generated blast shell compares to that of the ambient medium (Sorasio et al. 2006), and on the ratio of the amplitude of the shell's oscillation to it wavelength. It is thus difficult to obtain identical conditions in the simulation and experiment, which may explain the different growth rates of the NTSI.

The proton distribution in Figure 3(a) is not uniform along y and the accumulation of protons at the concave parts of the boundary at $(x, y) \approx (50, 50)$ and at $(x, y) \approx (150, 40)$ is evidence for a developing TSI (Dieckmann et al. 2015). The density of the thin shell has increased to values $\approx 3.3 n_0$ at the time 165 ps and it is no longer sinusoidal in Figure 3(b). The piecewise linear shape of the shell resembles the one in Dieckmann et al. (2015) after the thin-shell instability had saturated. Figure 3(c) shows that the oscillation amplitude has increased to over 11 μm. An almost linear growth of the amplitude, similar to the experiment, is observed during 35 ps $< t <$ 55 ps. The amplitude growth slows down after this time.

5. Summary

In conclusion, we report on the first observation of the NTSI in a laboratory experiment. The experimental data are in good agreement with analytical estimates and numerical simulations and provide the first proof of the existence of this instability in an early, pre-hydrodynamic, stage.

Strictly speaking, our experimental data only demonstrate that the NTSI can develop in a collisionless regime. However, since the redistribution of momentum within the thin shell is the driving mechanism for the NTSI in the collisionless and hydrodynamic cases alike, our experimental results also lend support to the existence of the hydrodynamic NTSI. Future experimental studies can follow the NTSI into the collisional regime and determine unambiguously whether or not it grows also in this limit.

An exciting feature of studying the NTSI with our experimental conditions is the resemblance of the laser-generated blast shell to the radially expanding blast shell of an SN. The growth of the NTSI and the evolution of the thin shell can thus be studied in a geometry that is similar to that of their counterparts in the blast shell of an SN and shed light on how the blast-shell flow is modified by this instability.

We acknowledge the contribution of the staff of the Central Laser Facility. We would also like to thank the EPSRC (EP/I031766/1, EP/K022415/1,EP/I029206/1), SFB-TR18, GRK1203, ENE2013-45661-C2-1-P, PEII-2014-008-P, Vetenskapsrådet (Dnr 2010-4063), and the Triangle de la Physique RTRA network (ULIMAC) for financial support and HPC2N (Umeå) for computer time. Data associated with research published in this Letter can be accessed at http://pure.qub.ac.uk/portal/en/datasets/experimental-observation-of-thinshell-instability-in-a-collisionless-plasma(587d02c0-9b5b-4d7a-84f8-6bdcf66e8a0d).html.

References

Ahmed, H., Dieckmann, M. E., Romagnani, L., et al. 2013, PhRvL, 110, 205001
Arber, T. D., Bennett, K., Brady, C. S., et al. 2015, PPCF, 57, 113001
Borghesi, M., Campbell, D. H., Schiavi, A., et al. 2002, PhPl, 9, 2214
Chevalier, R., Blondin, J. M., & Emmering, R. T. 1992, ApJ, 392, 118
Danson, C. N., Collier, J., Neely, N., et al. 1998, JMOp, 45, 1653
Dean, S. O., Mclean, E. A., Stamper, J. A., & Griem, H. R. 1971, PhRvL, 27, 487
Dieckmann, M. E., Ahmed, H., Doria, H., et al. 2015, PhRvE, 92, 031101

Dieckmann, M. E., Ahmed, H., Sarri, G., et al. 2013, PhPl, 20, 042111
Ditmire, T., & Edens, A. D. 2008, Laser Photon. Rev., 2, 400
Doria, D., Bret, A., & Dieckmann, M. E. 2016, arXiv:1611.04454
Edens, A. D., Ditmire, T., Hansen, J. F., et al. 2005, PhRvL, 95, 244503
Folini, D., Walder, R., & Favre, J. M. 2014, A&A, 562, A112
Gitomer, S. J., Jones, R. D., Begay, F., et al. 1986, PhFl, 29, 2679
Grun, J., Stamper, J., Manka, C., et al. 1991, PhRvL, 66, 2738
Heitsch, F., Slyz, A. D., Devriendt, J. E. G., Hartmann, L. W., & Burkert, A. 2007, ApJ, 665, 455
Hershkowitz, N. 1981, JGR, 86, 3307
Kirby, D., Green, S., Fiorini, F., et al. 2011, LPB, 29, 231
Kugland, N. L., Ryutov, D. D., Plechaty, C., Ross, J. S., & Park, H.-S. 2012, RScI, 83, 101301
Larsen, J. T., & Lane, S. M. 1994, JQSRT, 51, 179
McLeod, A. D., & Whitworth, A. P. 2013, MNRAS, 431, 710
Ryu, D., & Vishniac, E. T. 1987, ApJ, 313, 820
Sarri, G., Cecchetti, C. A., Romagnani, L., et al. 2010, NJPh, 12, 045006
Sarri, G., Dieckmann, M. E., Kourakis, I., & Borghesi, M. 2011, PhRvL, 107, 025003
Sorasio, G., Marti, M., Fonseca, R., & Silva, L. O. 2006, PhRvL, 96, 045005
Tan, T. H., McCall, G. H., & Williams, A. H. 1984, PhFl, 27, 296
van Marle, A. J., & Keppens, R. 2012, A&A, 547, A3
van Marle, A. J., Keppens, R., & Meliani, Z. 2011, A&A, 527, A3
Vishniac, E. T. 1983, ApJ, 274, 152
Vishniac, E. T. 1994, ApJ, 428, 186